J. Fluid Mech. (2007), *vol.* 592, *pp.* 135–154. © 2007 Cambridge University Press
doi:10.1017/S0022112007008324 Printed in the United Kingdom

Barotropically induced interfacial waves in two-layer exchange flows over a sill

M. ELETTA NEGRETTI[1], DAVID Z. ZHU[2] AND GERHARD H. JIRKA[1]

[1]Institute for Hydromechanics, University of Karlsruhe, Germany

[2]Department of Civil and Environmental Engineering, University of Alberta, Canada

(Received 24 November 2006 and in revised form 23 July 2007)

Two-layer exchange flows are observed in the channels/straits connecting two water bodies of different densities. This study examines the nature of the barotropic forcing and its effect on the interfacial waves in two-layer exchange flows over a smooth underwater sill. Experiments were conducted with different initial conditions, distinguishing the case of hydrostatic disequilibrium and the case of a global pressure-balanced state. The experiments demonstrate that the baroclinic exchange flow is dominated by the barotropic-forcing-induced oscillations. A simplified barotropic model is developed to predict the period of the barotropic oscillation with an excellent agreement with experimental measurements. Detailed velocity and flow-rate measurements also indicate the importance of the barotropic forcing in exchange flows. The effect of the superimposed barotropic forcing on the interfacial wave characteristics is also investigated. Large two-dimensional surge-like structures are observed during the experiments, whose generation is shown to be related to the flow-rate oscillations. The length scales of these structures is comparable with the total water depth and is shown to increase with increasing Reynolds numbers.

1. Introduction

Densities of natural water bodies such as oceans, estuaries and lakes can vary as a result of variations in temperature, salinity and/or sediment concentration. The density differences between neighbouring water bodies can drive flows in the connecting channel or strait. Examples of such flows are the exchange of Atlantic Ocean water with Mediterranean Sea water through the Strait of Gibraltar (Farmer & Armi 1988), or the exchange flows between the Baltic and the North Sea or through the Strait of Bosporus (Black and Mediterranean Seas). Exchange flows can also be driven by a small density difference between a lake and its embayment as a result of temperature differences, such as the exchange flow between Lake Ontario and Hamilton Harbor through the Burlington Ship Canal (Lawrence *et al.* 2004), and the exchange flows between different portions of a lake as in Lake Lucerne (Wüest, Imboden & Schurter 1988). In general, these flow processes are an interaction of purely baroclinic effects (due to density differences) and the associated interfacial instabilities, on one hand, and of additional barotropic components (due to various types of steady or unsteady external forcing), on the other hand. The key literature on these separate effects is reviewed in the following.

Armi (1986) studied the hydraulics of two-layer flows. He examined the concept of hydraulic controls (also called internal controls). Lawrence (1993) analysed

https://doi.org/10.1017/S0022112007008324 Published online by Cambridge University Press

theoretically and experimentally a steady two-layer flow past a fixed obstacle. Zhu & Lawrence (1998, 2000) extended the two-layer hydraulic theory by incorporating the non-hydrostatic pressure distribution due to streamline curvature and frictional effects.

At the interface of exchange flows, instabilities can develop, such as Kelvin–Helmholtz (KH) billows. Earlier studies have shown that the rates of the exchanges are controlled and/or influenced by the generation of these instabilities (Pratt 1987). The related flow entrainment has been shown to modify the density of the inflow and its eventual mixing and fate. Various review articles on mixing in stratified lakes and oceans (e.g. Thorpe 1985; Fernando 1991) document that hydrodynamic instabilities are largely responsible for the vertical mixing in the interior of oceans and lakes.

Morin, Zhu & Loewen (2004) studied interfacial KH instabilities in the supercritical region of two-layer exchange flows over a smooth bottom sill within the maximal exchange. They observed large periodic fluctuations in the measurements of the flow rate and the interface position and explained them as being caused by the generation of KH instabilities at the interface as well as by the internal seiche. Fouli (2006) studied experimentally the growth and development of the interfacial KH instabilities in a two-layer exchange flow over a sill. He observed a mechanism of entrainment and mixing during the maximal exchange, in which a low oscillation of the density interface and a shear generated KH instability above the sill crest led to the development of large-scale breaking waves.

However, the flow behaviour changes when steady or unsteady external forces are superimposed on the pure baroclinic flow. A series of papers by Farmer and Armi in the 1980s analysed the hydraulics of exchange and arrested flows, also through a contraction and a combination of a contraction and a sill, including results with a constant barotropic component. They showed that maximal two-way exchange with a net barotropic flow requires the presence of two controls, one at the narrowest and shallowest position and one more control, whose position depends on the barotropic force. Pawlak & Armi (1998, 2001) examined the vortex mechanisms developed in a stratified shear layer subject to spatial acceleration and the subsequent interfacial entrainment and mixing in their physical experiments in downslope currents, including results for flows with a superimposed weak and strong constant barotropic flow. They observed a mechanism of vorticity generation, where the core of the growing vortex was separated from the vorticity source and a second core developed. Finally, they showed that mixing induced by interfacial instabilities lead to the generation of a sharp density interface near the high-momentum stream.

Stommel & Farmer (1953) and Welander (1984) pointed out that barotropic current fluctuations can influence the amount of exchanged water masses as well as the mixing processes between the two layers, but none of them made a quantitative estimation of the effect. Stigebrandt (1977) developed a simple theory, showing that the two-layer transport capacity of a constriction may be increased considerably by barotropic current fluctuations. This was also confirmed by laboratory experiments. Helfrich (1995) examined numerically the effect of the time-dependence (e.g. tidal influence) on exchange flows. In his numerical solutions for both a pure contraction and an offset sill-narrows combination it was shown that the exchange flow, averaged over a tidal cycle, increased with the normalized velocity amplitude of the barotropic oscillation. The model results were compared to laboratory experiments for the pure contraction case and a good agreement for both interface evolution and average exchange was found.

In this paper, a stratified two-layer exchange flow over a submerged sill with a superimposed pulsating external forcing is studied experimentally, under conditions

https://doi.org/10.1017/S0022112007008324 Published online by Cambridge University Press

of higher Reynolds numbers than previous studies of co-current or countercurrent two-layer systems. Herein, the baroclinic component of the flow is obtained using different salt concentrations, while the pulsating external forcing (i.e. the barotropic component) is inevitably produced because of the starting conditions related to the experimental facility. In fact, the combined effects of baroclinic and unsteady barotropic components appear common in geophysical and environmental flows, as for example in sea straits, where metereological or astronomical tides are superposed on the baroclinic exchange flow or in exchange flows between two confined reservoirs (such as harbour oscillations) or different portions of a lake, where basin oscillations often occur, for example, owing to wind effects.

The superposed unsteady barotropic component has been shown to be responsible for the generation and development of large-scale two-dimensional structures at the interface between the two layers, in the form of surges. These large-scale billows have been previously observed by other authors having similar experimental conditions (Pawlak & Armi 2000; Morin *et al.* 2004; Fouli 2006).

In the present work, a theoretical approach has been used to predict the flow-rate oscillations and the related period, and the impact of the superimposed pulsating barotropic flow on the development of the shear interface is examined experimentally. A fundamental study of hydrodynamic instabilities at the interface of exchange stratified flows is important for modelling the vertical transport of heat, oxygen, nutrients and pollutants in lakes and oceans, as density stratification limits the vertical movement.

The paper is organized as follows. In § 2, the experimental set-up and techniques are described. The different starting conditions for the experiments are discussed in § 2.2. The theoretical approach predicting the flow-rate oscillations and the related period is presented in § 3.1. In § 3.2, the baroclinic flow with superimposed barotropic oscillation is described showing that significant effects are produced by the barotropic component. Further effects of the barotropic oscillation on the flow development and on interfacial wave characteristics are described in §§ 4.1 and 4.2. Section 5 summarizes the results.

2. Experimental design

2.1. *Experimental facility and techniques*

Experiments were conducted in a 12 m long and 0.6 m wide tank (figure 1), which is divided in the middle into two basins, and connected by a channel of reduced width (15 cm). The tank has a volume of 6 m^3, allowing a much wider range of flow conditions to be studied than in previous studies, in particular a longer experimental duration with larger Reynolds numbers. A bottom sill was placed in the channel whose shape is described by: $z(x) = h_s \cos^2(\pi x/(2L))$ for $-40 < x < 0$, and $z(x) = h_s - x/5$ for $0 < x < 100$, where $h_s = 20$ cm and $L = 100$ cm (see figure 1). A Plexiglas barrier was placed at the sill crest to divide the tank into two reservoirs. A desired buoyant acceleration was produced by adding salt (NaCl) to the water in the left-hand reservoir. Polyamide particles (PA12, Vestosint 2157) with a mean diameter of 200 μm and a density of 1.016 g cm^{-3}, were added in both reservoirs as tracer material for the velocity measurements with particle image velocimetry (PIV). A 10 W argon-ion laser (Stabilite 2016, Spectra-Physics lasers) operating in multimode ($\lambda_1 = 488$ nm, $\lambda_2 = 514$ nm) was used as a continuous light source. The beam was transmitted through a fibre optic cable to a line generator with spherical lenses (OZ Optics). The generated laser sheet at the sill crest had a breadth of approximately 2 m and a width of 5 mm

https://doi.org/10.1017/S0022112007008324 Published online by Cambridge University Press

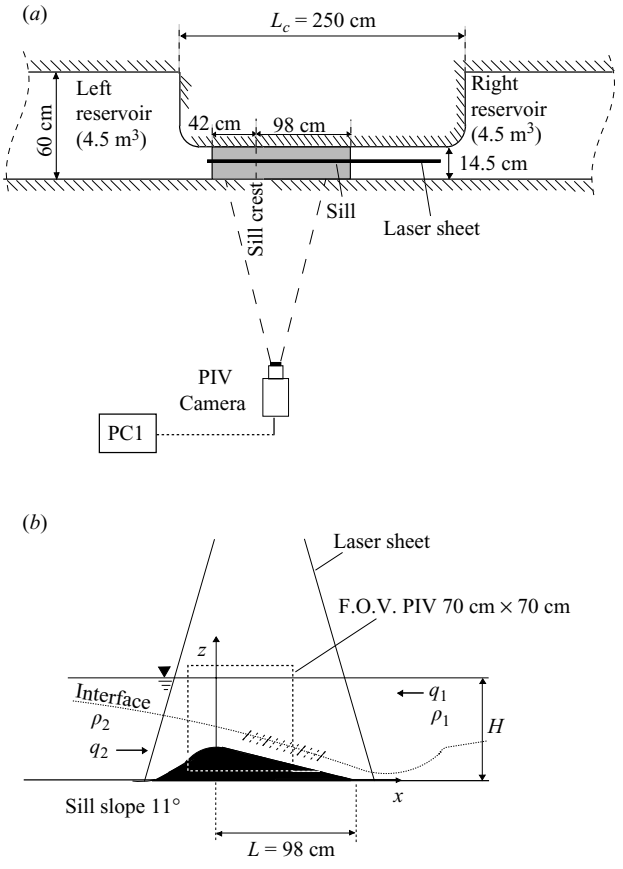


FIGURE 1. (*a*) Plan view and (*b*) side view of the experimental set-up. F.O.V. – field of view.

and was positioned in the middle of the channel. Images of 70 cm × 70 cm were grabbed with a CCD camera (FlowMaster 2, 8 bit, 1024 × 1024 pixels) at a frame rate ranging from 16 to 24 Hz. On the CCD camera, an optical lens was mounted along with a low-pass filter leading to a spatial resolution of 0.0625 cm/pixel. The 15 000 raw images were stored in real-time on a raid system. With the software package DaVis (LaVision) the velocity fields were computed using a cross-correlation PIV algorithm. For this purpose an adaptive multipass routine was used, starting with an interrogation window of 32 × 32 pixels and a final window size of 16 × 16 pixels with 50 % overlap. Each vector of the resulting vector field represents an area of roughly 0.6 cm × 0.6 cm. The velocity vectors were post-processed using a local median filter. Given the velocities encountered in the experiments, the experimental error in the instantaneous velocity is estimated to be approximately 3 %.

2.2. *Different starting conditions*

There are different possibilities for starting the experiments given the experimental facility described in the previous section. A first possibility, which has also been used in the majority of previous studies in stratified exchange flows, is to fill the tank to the desired water depth. After inserting a separating barrier to divide the tank into two reservoirs, a known amount of salt is added to one of the two reservoirs to generate the density difference. This configuration for the starting condition is shown

https://doi.org/10.1017/S0022112007008324 Published online by Cambridge University Press

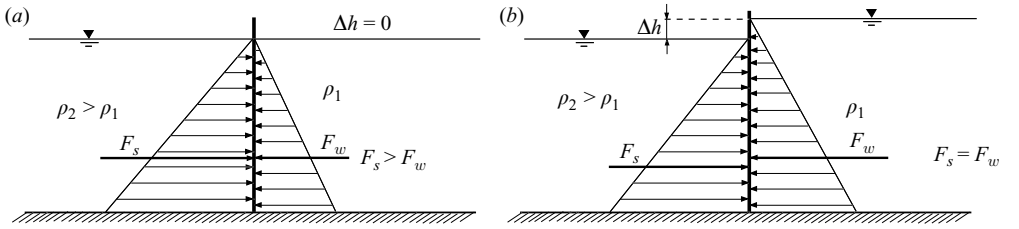


FIGURE 2. Sketch of different experimental starting conditions. (*a*) Hydrostatic pressure resultant force is unequal, but the water depths are at the same level. (*b*) Global balance equilibrium, but different water depths.

Exp.	g' (cm s^{-2})	H (cm)	f_{aq} (Hz)	Starting condition (figure 2)
1	3.09	40.5	16	(*a*)
2	3.09	51.0	20	(*b*)
3	3.09	59.7	20	(*b*)
4	5.81	41.0	10	(*b*)
5	5.81	61.0	16	(*a*)
6	0	40 + 2	24	(*b*)
7	0	40 + 6	24	(*b*)

TABLE 1. PIV-measurement program with the notations used: g' is the reduced gravity and H is the total water depth. Experiments 6 and 7 have been performed using only fresh water. f_{aq} represents the acquisition frequency. Finally, the possibilities shown in figure 2 for the starting conditions of the experiments are reported.

in figure 2(*a*). Referring to figure 2(*a*), if $\Delta h = 0$ as assumed for this first possibility, the density difference between the two reservoirs produces a net hydrostatic pressure force on the separating wall prior to the experiment beginning, i.e. $F_s > F_w$, in which F_s is the force on the partition from the salt-water side, and F_w on the fresh-water side. This initial global pressure unbalanced state generates a net flow through the flume in the longitudinal direction and thus an impulsive barotropic forcing. This results in an oscillation of the free surface, which will be superimposed onto the baroclinic exchange flow once the wall is removed, leading to wavelike responses.

Another possibile way to start the experiments is to add the corresponding volume of water in the fresh-water reservoir $\Delta h = h_2(\sqrt{\rho_2/\rho_1} - 1)$, with h_2 denoting the water depth in the reservoir filled with salt water and ρ_2 and ρ_1 being the density of the salt and fresh water, respectively. Thereby, a global balance equilibrium prior to the experiment beginning is established, i.e. $F_s = F_w$ (cf. figure 2*b*). In this second configuration, the unsteady barotropic component will be generated owing to the depth difference Δh at the beginning of the experiment: a surface wave will be created once the barrier is removed.

In the experiments, different methods were tried covering the above two extremes, including slow removal of the barrier. There are different ways to damp the barotropic oscillation. However, in all cases, the experimental evidence shows that there is no way to avoid completely the superposition of additional external forces on the baroclinic flow in experiments on two-layer exchange flows, given this experimental facility. Thus, careful attention should be paid in applying the different experimental starting conditions and their effects on the flow development should be carefully considered. Experiments 1 and 5 (table 1) were conducted using the first starting possibility discussed

https://doi.org/10.1017/S0022112007008324 Published online by Cambridge University Press

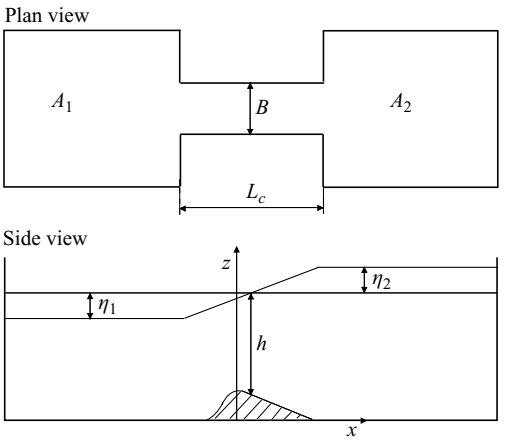


FIGURE 3. Sketch of the hydraulic system used for the model in § 3.1.

in § 2.2 (figure 2*a*), starting the experiment with the water depths in the left- and right-hand reservoirs at the same level. Experiments 2, 3 and 4 were conducted adding the corresponding amount of fresh water in the fresh-water reservoir, thus using the second starting possibility described in § 2.2 (figure 2*b*).

3. Unsteady start-up conditions and barotropic responses

3.1. *Simplified model of barotropic oscillations*

In this section a simplified model to study barotropically induced oscillations is derived,in an experimental two-basin set-up. The superimposed barotropic flow which is inevitably generated at the beginning of the experiment is also known as Helmholtz oscillation. The Helmholtz oscillation is characterized by a periodic mass exchange through a narrow strait and associated spatially uniform changes in the basins, representing a simple kind of resonance produced by an oscillatory external forcing. It would be useful to predict the oscillation periods and the flow rates, given the experimental conditions. For this purpose, the oscillating flow is considered as an unsteady one-dimensional flow between the two basins (figure 3). Neglecting in first order the viscous term, the momentum equation for the horizontal velocity component u is

$$\frac{\partial u}{\partial t} + u\frac{\partial u}{\partial x} = -\frac{1}{\rho}\frac{\partial p}{\partial x}. \tag{3.1}$$

Assuming that the volumes of the basins are much larger than that of the channel, the two basins are related by

$$A_1\eta_1 = -A_2\eta_2, \tag{3.2}$$

where A_1 and A_2 are the basin areas and η_1 and η_2 are the free-surface displacements with respect to the still-water elevation. The continuity equation is

$$A_2\frac{\partial \eta_2}{\partial t} = qB, \tag{3.3}$$

where q is the flow rate per unit width and B is the width of the channel, assumed constant. Assuming a small surface deflection, η_1 and $\eta_2 \ll h$, the momentum equation (3.1) becomes

$$\frac{1}{h}\frac{\partial q}{\partial t} + \frac{q}{h}\frac{\partial (q/h)}{\partial x} = -\frac{1}{\rho}\frac{\partial p}{\partial x}. \tag{3.4}$$

https://doi.org/10.1017/S0022112007008324 Published online by Cambridge University Press

The pressure gradient is represented by a linear free-surface deflection

$$\frac{\partial p}{\partial x} = \frac{(\eta_2 - \eta_1)\rho g}{L_C} = \frac{\eta_2(1 + A_2/A_1)\rho g}{L_C}, \tag{3.5}$$

where L_C is the length of the connecting channel. Equation (3.4) becomes

$$\frac{1}{h}\frac{\partial q}{\partial t} + \frac{q}{h}\frac{\partial (q/h)}{\partial x} = -\frac{g\eta_2(1 + A_2/A_1)}{L_C}. \tag{3.6}$$

Differentiating (3.6) with respect to time, we finally obtain

$$\frac{1}{h}\left[\frac{\partial^2 q}{\partial t^2} - \left(\frac{2}{h^2}\frac{\mathrm{d}h}{\mathrm{d}x}\right) q\frac{\partial q}{\partial t}\right] = -\frac{gqB(1 + A_2/A_1)}{L_C A_2}. \tag{3.7}$$

At the sill location, $\mathrm{d}h/\mathrm{d}x = 0$, (3.7) reduces to the wave equation

$$\frac{\partial^2 q}{\partial t^2} + \left[\frac{ghB(1 + A_2/A_1)}{L_C A_2}\right] q = 0. \tag{3.8}$$

The general solution is then given by:

$$q(t) = A\sin(\omega t + \phi), \tag{3.9}$$

where $\omega = \sqrt{k}$, $k = ghB(1 + A_2/A_1)/(L_C A_2)$, and ϕ is the initial displacement, which can be set to zero with the initial condition $q|_{t=0} = 0$. The associated period is given by:

$$T = \frac{2\pi}{\omega} = 2\pi\sqrt{\frac{L_C}{g(1 + A_2/A_1)}\frac{A_2}{Bh}}. \tag{3.10}$$

Equation (3.10) can be rearranged to give

$$T = \frac{2\pi L_C}{\sqrt{ghA_C\dfrac{A_1 + A_2}{A_1 A_2}}}, \tag{3.11}$$

where $A_C = L_C B$ is the surface area of the channel. If $A_1 \gg A_2$ (or $A_2 \gg A_1$), like the connection between the ocean and a harbour, the above equation can be further simplified.

Equation (3.11) is derived assuming that the water level in both tanks rises and falls in unison. In this study, the disturbance starts from the channel, and it travels through the tank before it is bounced back. This suggests that the period should be increased by a factor which accounts for the time taken by the gravity wave to reach the end of the channel. This correction could be made by using, for example, a larger length of the channel and reduced areas for the reservoirs. On the other hand, the velocity in the channel, which is proportional to $\sqrt{gh}$, is higher than assumed in the model, as we assume the smallest water depth h at the sill crest, and this might compensate for the assumption of unison rise and fall of the water levels in the reservoirs. The very good agreement of the observed periods with the periods predicted by (3.11) presented in the next section will confirm this.

Finally, we expect that in addition to the above frequency, other higher frequencies will be present owing to the limited dimensions of the tank (sidewall effects), which can be calculated by the classical relations valid for harbour hydrodynamics theory (see for example Dean & Dalrymple 1984) as well as lower frequencies related to internal seiches. In the following sections, it is shown that owing to the starting conditions

https://doi.org/10.1017/S0022112007008324 Published online by Cambridge University Press

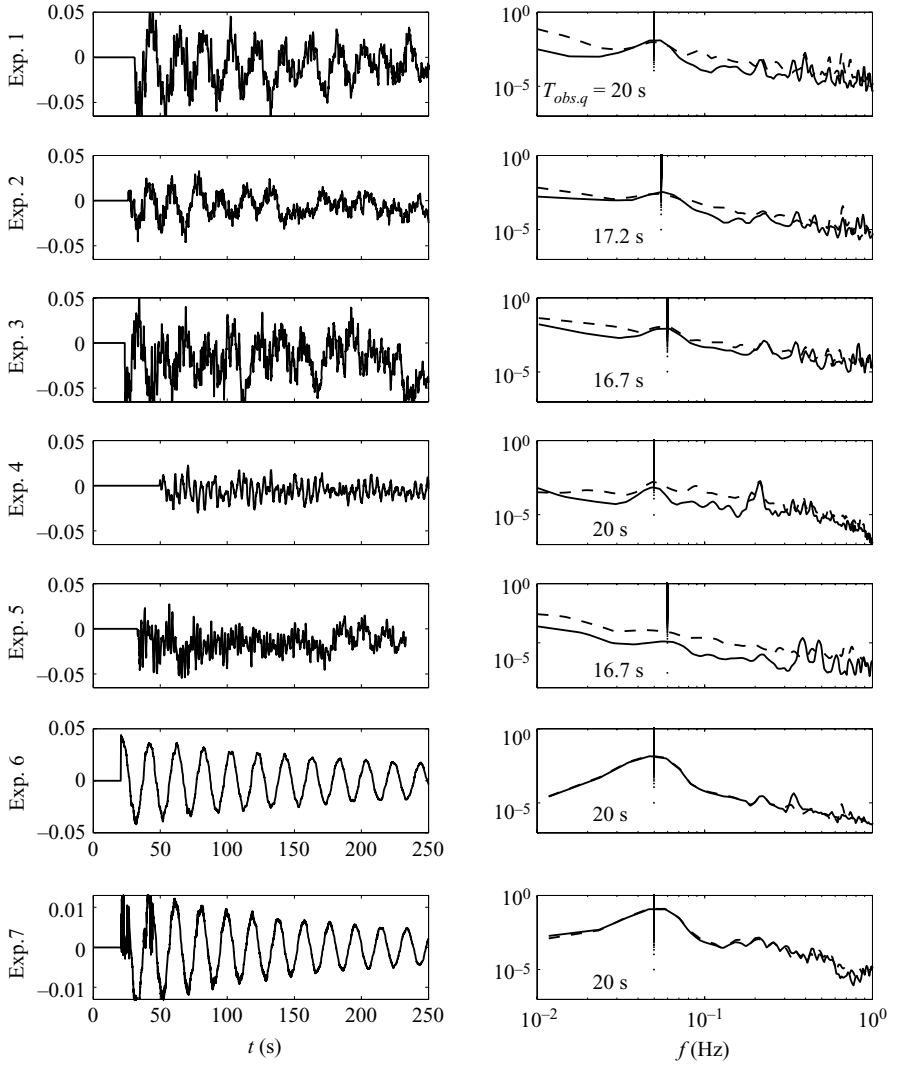


FIGURE 4. Normalized net flow rate per unit width approximately at the sill crest (continuous lines) and at $x/L = 0.4$ (dashed lines) plotted over time (a) with relative spectral distribution (b) for all the experiments. In experiments 6 and 7 the net flow rate is normalized with the acceleration due to gravity g.

described above and to the resulting unsteady barotropic forcing, significant effects are generated on the exchange flow.

3.2. *Barotropic oscillation in the exchange flow*

In the following, the vertical lengths are non-dimensionalized with the total water depth H while the horizontal lengths are non-dimensionalized with the length of the sill on the right-hand side of the sill crest L (see figure 1b) and the channel width B. The origin of the longitudinal coordinate is posed at the sill crest. Moreover, the velocity scale is given by $\sqrt{g'H}$ and the per unit width flow-rate scale by $H\sqrt{g'H}$. For the data processing, 5 000 images were used. In figure 4(a), the normalized total flow rate approximately at the sill crest per unit width is plotted over time for all the

https://doi.org/10.1017/S0022112007008324 Published online by Cambridge University Press

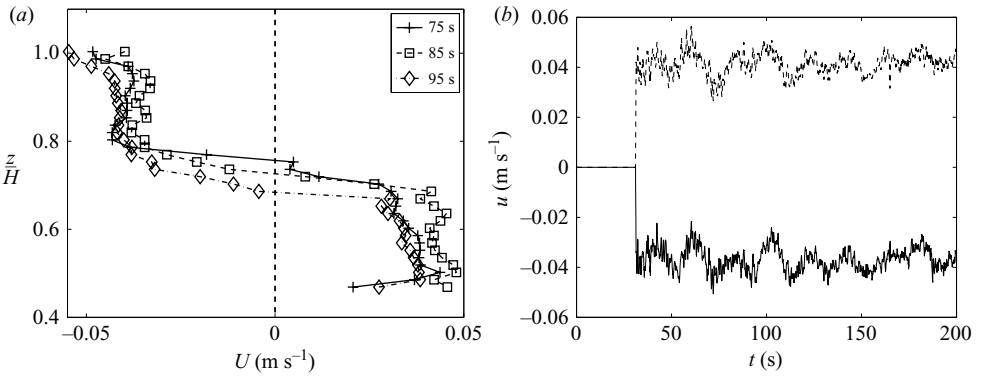


FIGURE 5. (*a*) Velocity profiles at the sill crest for experiment 1. The time steps are 10 s. The profiles translate in the longitudinal direction, thus suggesting that barotropic forces are responsible for the flow-rate oscillations. (*b*) Time series at the sill crest of the horizontal velocities in the upper (continuous line, at $z/H = 0.875$) and lower (dashed line, at $z/H = 0.625$) layer. The time series of the velocities in the upper and lower layer are in phase, thus showing that the oscillations are caused by barotropic forces rather than by internal seiches, in which case they would be out of phase.

experiments performed. In experiments 6 and 7, the net flow rate is normalized with the acceleration due to gravity g. For all the experiments performed, the flow rate is oscillating in time around a zero value, thus indicating a net flow oscillating periodically from one side to the other, independent of the chosen method for the experimental starting conditions. The amplitude of these oscillations is decaying in time because of frictional effects. In figure 4(*b*), the spectral distribution of the net flow rates at the sill crest are shown, with dominant periods $T_{obs,q}$. From figure 4, it appears that these frequencies are caused by the influence of the pulsating barotropic component, because they are equal for each experiment with the same water depth H and do not depend on the buoyant acceleration. This is additionally proved by considering figure 5(*a*) which gives the time-shifted velocity profiles at the same location for experiment 1: baroclinic effects would result in a change in the area of the velocity profiles between the upper and lower layers, while barotropic effects would cause a translation in longitudinal direction of the entire profile in time. Figure 5(*a*) shows that the profiles translate in the streamwise direction.

Spectral analysis was also conducted on the time series of the shear interface, here defined as $(h|_{\overline{u}=0.85} + h|_{\overline{u}=0.15})/2$, where $\overline{u}$ is the normalized velocity profile with $\overline{u} = 0$ and $\overline{u} = 1.0$ for the minimum and maximum velocity, respectively. At the sill crest, low frequencies could be observed and the corresponding periods ($T_{obs,i}$) are also resumed in table 2 along with the periods observed also by Morin *et al.* (2004). From table 2, we can see that the periods of oscillation of the interface are slightly different from those of the net flow rate. This difference in the periods of the oscillation of the interface and flow rate has been observed by Morin *et al.* (2004) (cf. table 2), and can be explained as follows: the oscillation in the net flow rate is controlled by the translation motion of the fluid through the channel. The fluctuations of the interface, however, are the result of two mechanisms, namely surge-like accumulations at the sill crest triggered by the barotropic flow and the additional baroclinic wave growth at the interface (i.e. even for steady exchange flow). As can be seen in table 2, apparent nonlinear interaction between these mechanisms causes a shorter interfacial wave period $T_{obs,i}$ as opposed to the pure barotropic flow fluctuation period $T_{obs,q}$.

https://doi.org/10.1017/S0022112007008324 Published online by Cambridge University Press

	$H-h_s$ (cm)	$T_{obs.i}$ (s)	$T_{obs.q}$ (s)	$T_{Eq.(3.11)}$ (s)	$\frac{T_{obs.q}-T_{obs.i}}{T_{obs.q}}$ (%)
Morin *et al.* (2004)	20	14–24	14–17	14.5	15.4
This study	20	16.7	20.0	22.5	16.5
	30	14.3	17.2	18.3	16.8
	40	13.3	16.7	16.2	20.3

TABLE 2. Comparison between the observed periods in the spectral distribution of the experimental net flow rate ($T_{obs,q}$) for this study and Morin *et al.* (2004) and the predictions by the theoretical model presented here for the experimental data ($T_{Eq.(3.11)}$). The experimental periods of the flow rate are also compared to those observed in the spectral distribution of the interface position ($T_{obs,i}$) showing discrepancies ($(T_{obs,q}-T_{obs,i})/T_{obs,q}$). h_s represents the height of the sill crest.

The flow rate driven by the barotropic forcing due to the initial experimental conditions can be computed and compared with the measurements. The corresponding Δh due to the density difference is 0.18 cm and 0.12 cm for experiments 1 and 3, respectively. The volume difference between the two tanks is $\Delta h A_1 = 3.6$ l and 5.4 l, respectively. This volume difference can drive the flow rates $q = 0.36\,\mathrm{l\,s^{-1}}$ and $q = 0.6\,\mathrm{l\,s^{-1}}$, respectively, if the volume is divided by half of the barotropic oscillation period $T_{obs,q}$ (cf. figure 4*b*). The normalized flow rates ($q/\sqrt{g'\overline{H}HB}$) give 0.055 and 0.051, respectively, which compare well with the flow-rate amplitudes plotted in figure 4(*a*) for experiments 1 and 3.

In experiments 6 and 7, both basins were filled with fresh water and with a depth difference Δh of 2 cm and 6 cm, respectively, across the barrier between the two basins. The time series of the net flow rate per unit width at the sill crest and the spectral distributions for experiments 6 and 7 are presented in figure 4. Again, the same peaks for these two experiments can be recognized as compared to the other experiments with a density difference. The volume difference between the two tanks is $\Delta h A_1 = 60$ l and 180 l, respectively, which can drive normalized flow rates $q/(Bg) = 0.0042$ and 0.013 for experiments 6 and 7, respectively. These values are again comparable to the amplitudes plotted in figure 4. Figure 4 for experiments 6 and 7 also shows that the depth difference Δh does not influence the frequency, but only the amplitude of the oscillation. It is also worth noting that in experiments 6 and 7 the mean value of the flow rate is zero, while in the other experiments the mean value seems to be negative, i.e. more fresh water is flowing from right to left as salt water flows from left to right. This is probably due to three-dimensional effects and to the difficulty in resolving the lower-layer velocity.

A comparison between the periods observed in the flow-rate oscillation in the experiments performed in this study, and the periods observed by Morin *et al.* (2004), with the periods given by (3.11) is given in table 2 and it shows excellent agreement. In our experimental facility, the sill height h_s is given by 0.2 m, $A_1 = A_2 \approx (0.6 \times 5)\,\mathrm{m^2} = 3\,\mathrm{m^2}$, $B = 0.145$ m and $L_C = 2.5$ m.

Another proof to show that the oscillations in the flow rate are caused by barotropic forces rather than by internal seiches is given in figures 5(*b*), where the time series of the instantaneous horizontal velocities in the lower (continuous lines, at $z/H = 0.875$) and upper (dashed line, at $z/H = 0.625$) layer at the sill crest are plotted for experiment 1. The time series of the velocities in the upper and lower layer are in phase:

https://doi.org/10.1017/S0022112007008324 Published online by Cambridge University Press

for internal seiches they would be out of phase. It is of interest to compare the above frequencies with those of basin internal seiches. As described by Morin *et al.* (2004), an approximate estimate of the seiche period can be obtained assuming the reservoir is a closed two-dimensional basin with a length $L_{tot} = 12$ m. The propagation speed of the internal interfacial wave is given by $c = \sqrt{g' z_1 z_2/(z_1 + z_2)}$, where z_1 and z_2 are the water depths of the lower and upper layer, respectively. The fundamental mode of the internal seiche has thus a period of $T_s = 2L_{tot}/c$. Assuming the interface is at the middle depth of the reservoir, i.e. $z_1 = z_2$, the periods of the internal seiche are given by $T_s = 610$ s, 498 s, 432 s, 445 s and 315 s for experiments 1, 2, 3, 4 and 5, respectively. The peaks relative to these periods cannot be seen in figure 4 because the steady period duration of the experiments is similar to that of the internal seiche, so that not enough data for the spectral analysis is available.

Finally, it is observed that as an additional effect, the superposed barotropic oscillation influences the properties of the flow regimes: generally, for purely baroclinic flows, the maximal exchange regime is steady, but in the case of superimposed pulsating barotropic flow, the maximal exchange regime becomes periodic.

The generated barotropic oscillations are not only an artefact due to the chosen experimental design: such oscillations appear ubiquitous in environmental and coastal engineering as the basin oscillations between the different portions of a lake (such as Lake Lucerne in Switzerland, Wüest *et al.* 1988) or harbour oscillations. In these examples, the barotropic component can be caused under the action of surface wind and the periods of oscillations are determined by the geometry of the basins and are of the same order of magnitude as the periods encountered in our experiments. Barotropic oscillations also appear common in oceanography, i.e. in sea straits, or in atmospheric flows as mountain downslope winds, and are caused by astronomical or metereological tides. In these cases, however, the period is not determined by the geometrical features of the basins, as they can be assumed as infinitely large, but by the tide period. These periods are significantly larger than those encountered in our experiments: for example, using a water depth of 500 m as typical in the Strait of Gibraltar or in the Faroe Bank Channel, the periods in nature are 50 times larger than the periods in these experiments. Nonetheless, the effects of this barotropic oscillation on the exchange flow and on the interfacial wave characteristics cannot be neglected, as also demonstrated by the field observations of Sherwin & Turrell (2005) (see also Hansen & Osterhus 2000).

In the next section, the effect of the superposed pulsating barotropic component is analysed in more detail with respect to the interfacial wave characteristics, as described qualitatively in § 4.1. With this aim, results from experiments 1, 2, 3, 4 and 5 of the PIV measurements are further discussed in the following.

4. Effect of the barotropic oscillation on interfacial waves

4.1. *Visual observations and qualitative description of the flow*

When the separating wall is removed, an exchange flow commences. After an initial unsteady period (here of about 1 min), a maximal exchange regime is established (Armi 1986; Zhu & Lawrence 1998; Morin *et al.* 2004) with two internal controls, one at the sill crest, the other at the channel exit. In the last part of the experiment, the flow becomes unsteady again owing to the loss of one control (at the channel exit) and the sub-maximal exchange, characterized with a decreasing flow rate, starts. Here, only results of PIV experiments in the (periodic) maximal exchange regime are considered. Figure 6 shows a series of instantaneous pictures (with a time interval of 2 s)

https://doi.org/10.1017/S0022112007008324 Published online by Cambridge University Press

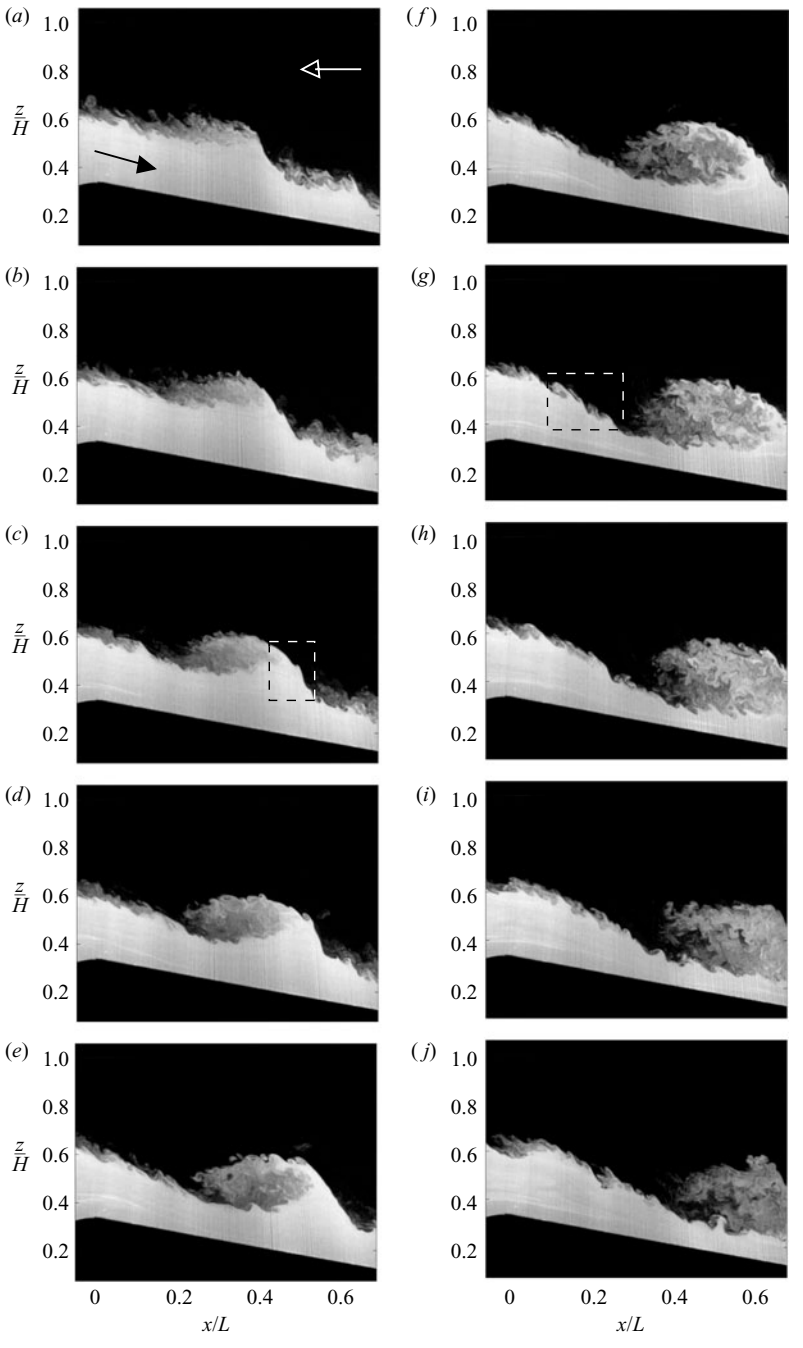


FIGURE 6. Series of images taken 3 min after the beginning of the experiment (experiment 3) with Rhodamine diluted in the salt-water layer flowing from left to right. The interval between successive images is 2 s. The image is 56 cm vertical and 70 cm horizontal. In (*c*) and (*g*), the dashed squares represent the enlargements in figures 7(*a*) and 7(*b*), respectively.

for experiment 3, in which Rhodamine 6G is mixed in the salt water, 3 min after the beginning of the experiment. At the beginning of this cycle, the interface position at the sill crest increases and is advected downstream (see figure 6*a*). In this region, where

https://doi.org/10.1017/S0022112007008324 Published online by Cambridge University Press

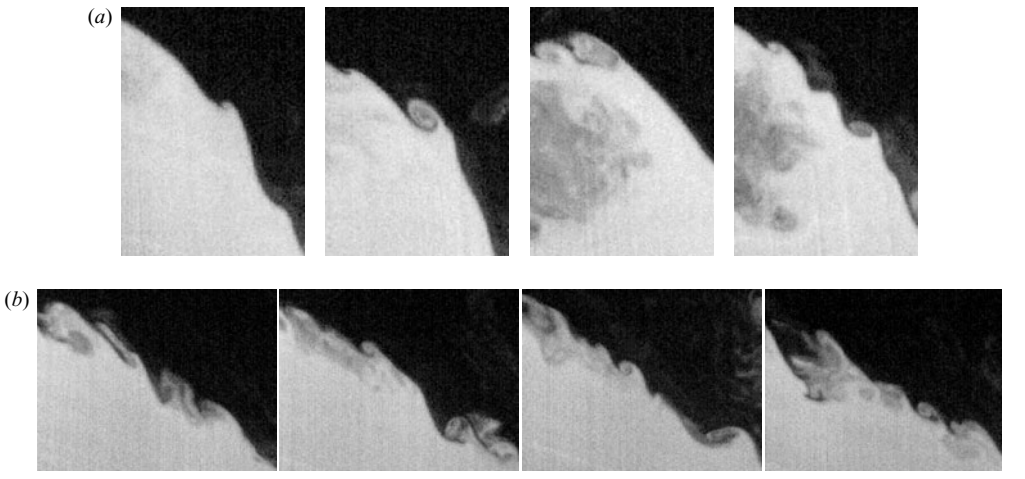


FIGURE 7. (*a*) Enlargement of the front of the billow in figure 6(*c–f*), and (*b*) of the sharp interface in the wake directly behind the billow in figure 6(*g–j*). The image is (*a*) 10 cm (vertical) by 6 cm (horizontal) and (*b*) 6 cm by 15 cm, respectively.

the velocity difference between the upper and lower layers is increasing owing to the accelerating flow down the sill, the formation of a large-scale billow can be observed at approximately $x/L = 0.25$ (see figure 6*b–d*). This billow is advected downstream and grows further, entraining significant fresh water into the core of the billow, at the same time carrying salty water from the lower layer to higher water depths, where it can be mixed with the fresh water in its core (see figure 6*e*, *f*). Until this point, a very sharp interface is created on the front (on the right) of the billow, where small-scale KH billows are generated (cf. figure 7*a*). In figure 6(*g*), the billow starts to collapse, creating a sharper interface upstream, characterized again by the formation of small-scale KH billows. Meanwhile the interface at the sill crest sharpens again and produces at the front of the wave further KH instabilities (see figure 7*b*), while the old billow continues to decay as it is stretched and further advected downstream. The high interface front at the sill crest is then advected down the sill (figure 6*j*) and the phenomenon starts again from the beginning as in figure 6(*a*). The KH instabilities generated at the sill crest are advected in both down and upstream directions.

These large-scale billows, which are periodically generated during the maximal exchange regime have also been seen in similar laboratory experiments by previous authors (e.g. Pawlak & Armi 2000; Morin *et al.* 2004; Fouli 2006), although their generating mechanism has apparently not been identified and analysed in detail. From experimental observations, the generation period of these large-scale interfacial instabilities is of the same order as the period of the barotropic flow-rate oscillations, depending on the Reynolds number. A possible physical explanation for the observed large-scale billows consists in considering them as a series of surges that lead to a pulsating density current in the lower layer, superposed to a base flow (see figure 8). These surge-like elements are generated periodically at the sill crest to ensure that the barotropic induced overflow can be exchanged from one reservoir to the other. These surges act similarly to thermals on a sloping bottom (see for example Turner 1963). Also, there is a strong similarity of these pulsating surge-like flows with roll waves in single-layer flows, which are explained in Baines (1995) as a sequence of periodic hydraulic jumps propagating down a slope. This type of wave has been observed

https://doi.org/10.1017/S0022112007008324 Published online by Cambridge University Press

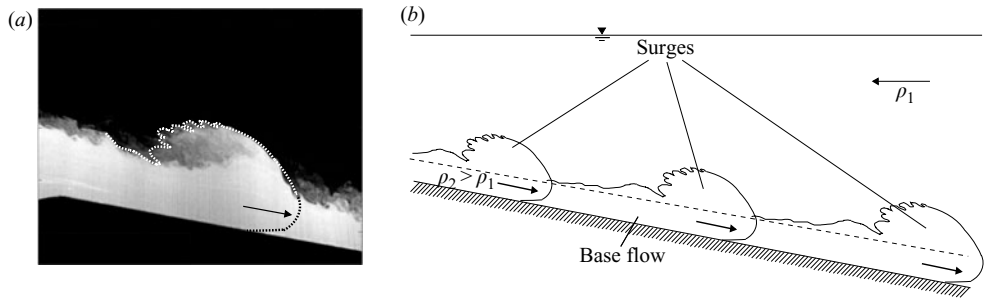


FIGURE 8. Physical explanation of the large-scale wave mechanism observed during the experiments. (*a*) Instantaneous image (in figure 6*c*) with a surge-like flow sketched onto the picture (dashed lines). (*b*) Schematization of the exchange flow down the sill with periodic surge formation to balance the barotropic generated overflows.

in atmospheric flows, for example in downslope windstorms in Boulder, Colorado (Scinocca & Peltier 1989).

4.2. *Interfacial wave characteristics*

Spectral distributions of the velocity fluctuations were calculated from the velocity fields obtained from the PIV measurements in order to gain an overview of the scales dominating the flow. These energy spectra give only qualitative estimations of spectral slopes and behaviours owing to the relatively low acquisition frequency and spatial resolution of the PIV experiments. Figure 9 shows representative energy spectra of the velocity fluctuations of the main velocity component (continuous line) and of the vertical velocity component (dashed line) at $x/L = 0.2$. Slopes of $-7/3$ and -2 are shown for comparison along with the typical turbulent spectral slope of $-5/3$. The spectral slope is a measure of the rate of energy transfer between the scales since the Reynolds number is large enough. For all experiments, the first part of the spectrum seems to be described better by a $-7/3$ or a -2 slope. The classical $-5/3$ slope characterizes more the last part of the spectrum up to frequencies of 2×10^0.

An important issue in the study of stratified flows is to separate the large-scale generated frequencies caused for example by internal waves, and the contribution by the buoyancy-driven small scales. Low-frequency ranges in stratified flows have been shown to be better described by -2 and $-7/3$-slopes, for frequencies usually lower than the (bulk) buoyancy frequency $N = g'/\delta$ (Lien, D'Asaro & Dairiki 1998), where δ is the shear-layer thickness which will be defined below. In this zone of the spectrum, the velocities are anisotropic, as also demonstrated by the difference in the spectrum of the horizontal and vertical components of the velocity: first, the slopes in the spectra of the vertical component of the velocity (dashed lines in figure 9) for all the experiments seem, from the beginning, to be better described by a $-5/3$ slope. Secondly, the effect of buoyancy can be seen in the vertical velocity fluctuations at the larger scales where the energy is approximately one order of magnitude less than that of the streamwise fluctuations. For increasing frequencies, the velocities become nearly isotropic and the spectral slopes for the horizontal component of the velocity decrease to the $-5/3$-slope, characterizing the small-scale buoyancy dominated turbulence.

Despite the fact that at these scales the limits of the PIV averaging become significant, the energy in the last part of the spectrum shows a distinct separation, which is remarkable for experiments 1, 2 and 3 and is much weaker for experiments 4 and 5 characterized with a higher buoyancy, where the spectra of the streamwise

https://doi.org/10.1017/S0022112007008324 Published online by Cambridge University Press

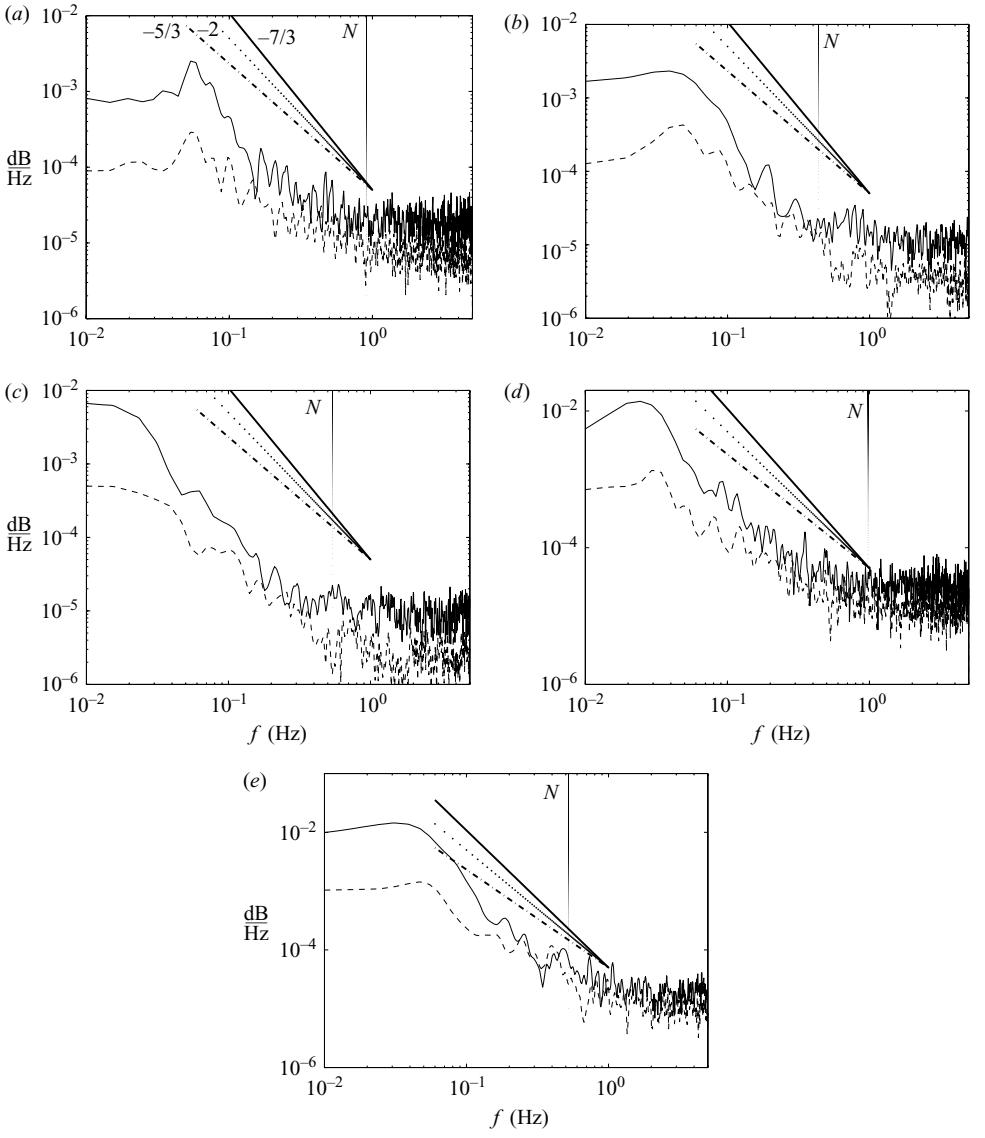


FIGURE 9. Spectral distribution of the instantaneous velocity fluctuations in the streamwise (continuous line) and in the vertical direction (dashed line) at the interface position at $x/L = 0.2$ for experiments 1 (*a*), 2 (*b*), 3 (*c*), 4 (*d*) and 5 (*e*). Spectral slopes of $-7/3$, -2 and $-5/3$ are plotted for comparison along with the buoyancy frequency N. The spectra of the vertical velocity fluctuations are one order of magnitude lower than those of the horizontal component for low frequencies. Moreover, the two spectra coalesce earlier for the experiments with higher buoyant acceleration, (*d*) and (*e*).

and vertical velocity components coalesce very early, at approximately $f \sim N$. For the first three experiments, the gap between the two spectra remains nearly constant for the whole range of frequencies. This is probably due to the increasing Reynolds number (see table 1), which inhibits the stabilizing effect of buoyancy (see table 1). For comparison, the buoyancy frequency N is also plotted in figure 9.

https://doi.org/10.1017/S0022112007008324 Published online by Cambridge University Press

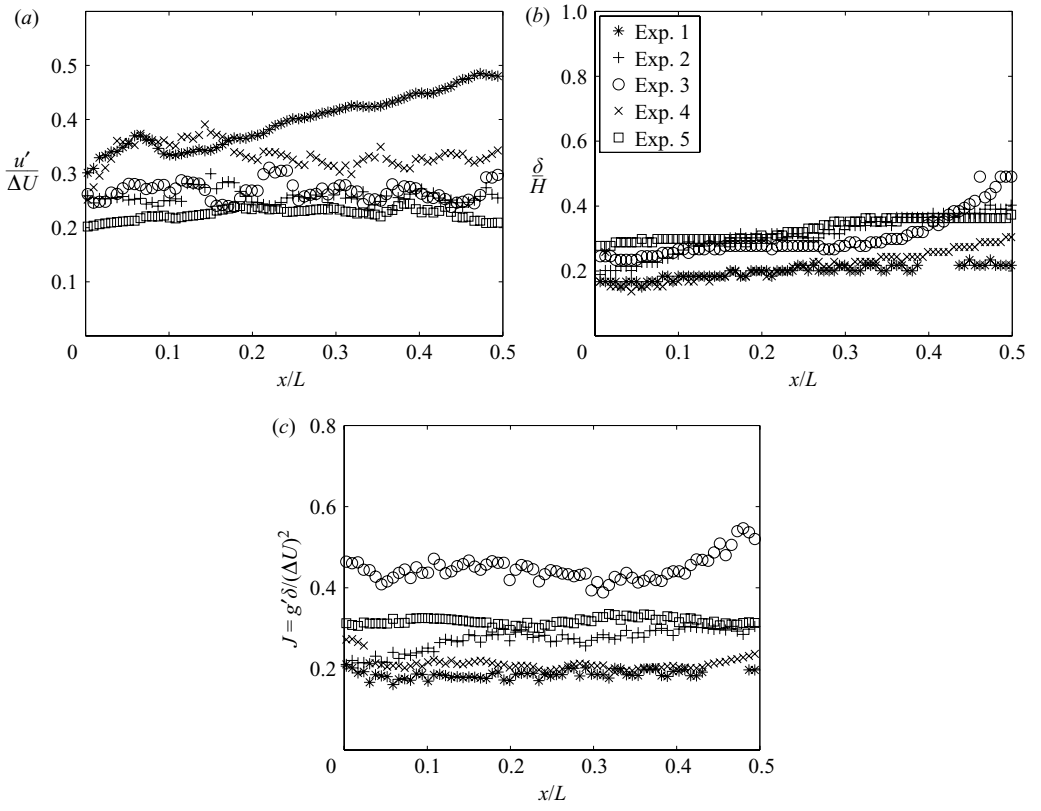


FIGURE 10. Time-averaged quantities for all the performed experiments. (*a*) Maximal r.m.s. of the streamwise velocity component normalized with the local maximal velocity difference *vs.* x. (*b*) Shear-layer thickness and (*c*) bulk Richardson number *vs.* x.

The streamwise root mean square (r.m.s.) velocity fluctuation u' downstream of the sill crest is shown in figure 10(*a*), normalized with the local velocity difference ΔU. This ratio gives the response of the velocity fluctuations to the velocity difference increase due to the acceleration down the sill. The level of this velocity fluctuation, $u'/\Delta U$, is higher than 0.2 for all the experiments. This is significantly larger than those generated by turbulent jets. The reason for the large u', at least partly, is the low-frequency oscillations caused by barotropic forcing. In experiments 2, 3, 4 and 5 the ratio remains nearly constant. In experiment 1, with the lowest Reynolds number, the ratio is slightly increasing. Koop & Browand (1976) and Pawlak & Armi (2000) reported a decay of this ratio in the longitudinal direction of $x^{-3/4}$ as an indicator of collapse of the initial turbulence in the shear layer. This is not observed here, as the increasing Reynolds number in the accelerating rapid-growth region right to the sill crest, results in an input of energy, thus keeping the ratio nearly constant.

The mean shear-layer thickness was defined as $\delta = h|_{\overline{u}=0.15} - h|_{\overline{u}=0.85}$. The mean shear-layer thickness along the longitudinal direction is plotted in figure 10 (*b*). The increase for experiments 1 and 4 is linear and almost equal for both. It is also worth noting that an increase of the water depth causes the shear-layer thickness to grow faster, whereas an increase of the buoyant acceleration results in a slightly slower growth of the shear layer. This is obviously due to the buoyancy, inhibiting the vertical motion. The bulk Richardson number is here defined using the velocity shear-layer

https://doi.org/10.1017/S0022112007008324 Published online by Cambridge University Press

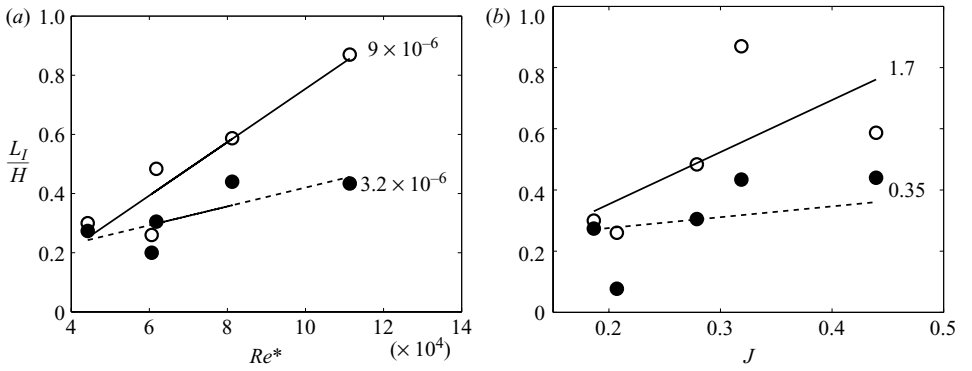


FIGURE 11. Estimation of the length scales of the large structures observed in the experiments. (*a*) Estimated length scales from the correlation functions of the horizontal (open symbols) and of the vertical (filled symbols) length scales *vs.* the overall Reynolds number $Re_* = \sqrt{g'H}H/\nu$ and (*b*) *vs.* the overall bulk Richardson number $J = g'\delta/(\Delta U)^2$, averaged in the range $0 \leqslant x/L \leqslant 0.4$.

thickness, $J = g'\delta/\Delta U^2$, (see figure 10*c*). For all the experiments, it remains nearly constant and it ranges from 0.2 for experiments 1 and 4 to 0.5 for experiment 3. These averaged quantities of the mean shear-layer thickness and Richardson number are of interest for the discussion on the length-scale estimation of the large-scale interfacial structures.

For the estimation of the length scales of these structures, the temporal correlation functions $R(\tau)$ of the horizontal and vertical velocity components have been determined. The length scales were then calculated as a product between the time scale $T_I = \int_0^\infty R(\tau)\,\mathrm{d}\tau$ and a convective velocity scale, here assumed to be half of the velocity difference $\Delta U/2$.

One fundamental issue in the investigation of interfacial instabilities in stratified exchange flows is the determination of the key parameters governing the generation, the growth and development of these instabilities. They are the result of an interplay between buoyancy and the mean shear velocity for a constant slope of the sill. As the flow treated here is also governed by barotropic forces, we expect that the water depth is playing a crucial role in determining the size of these instabilities. Thus, we argue that the key parameter governing the generation and development of these surge-like waves is the water depth H. The buoyancy seems to have a secondary importance in influencing the size of these instabilities at the interface. In this sense, a Reynolds number defined using the velocity scale $\sqrt{g'H}$ and as length scale the water depth H, i.e. $Re_* = \sqrt{g'H}H/\nu$, should be an appropriate parameter to illustrate the development of the length scales of such waves in a stratified exchange flow with superposed pulsating barotropic forcing, as first, the effects of changes in the water depth are taken into account and, secondly, the effects of buoyancy.

In figure 11(*a*), the horizontal (open symbols) and vertical (filled symbols) length-scale estimations are plotted versus the Reynolds number. Both the vertical and horizontal estimated length scales show overall increasing values with increasing Re_*. If the data are fitted with a linear curve, a slower increase for the vertical scales can be seen. This is obviously due to the buoyancy, which inhibits vertical motion. On increasing the buoyant acceleration (experiments 1 to 4 and experiments 3 to 5), the estimated length scales are not increasing, but remain constant or decrease. This is observed for values of the Reynolds number smaller then approximately 0.6×10^5.

https://doi.org/10.1017/S0022112007008324 Published online by Cambridge University Press

At this value, there is an abrupt increase of the size of the scales with increasing Reynolds number, and the buoyancy seems to alleviate this stabilizing effect. We thus propose a relation between the Reynolds number Re_* and the length scales of the large-scale surges,

$$\frac{L_I}{H} = \kappa Re_*,$$

where κ is 3.2×10^{-6} for the vertical scales and 9×10^{-6} for the horizontal scales. More precise estimations of the value of the constant κ should be achieved through additional experiments. For all experiments, the horizontal scale is larger than the vertical scale. The vertical scales are shown to be approximately $1/3$ of the total water depth for experiments 1 and 2, whereas they are roughly $1/2$ for experiments 3 and 5 and $1/4$ for experiment 4. Also the results for the horizontal length scales are consistent with the experimental observations presented in § 4.1.

If the scales are plotted *vs.* the Richardson number, no firm conclusions about a tendency are possible, as shown by the larger difference between the experimental data and the linear fit in figure 11(*b*) as compared to figure 11(*a*). The bulk Richardson number is a measure of the stabilizing effect of buoyancy relative to the destabilizing effect of the mean shear. Changes in the bulk Richardson number are primarily the result of changes in the buoyant acceleration. As mentioned above, a change in the buoyant acceleration produces changes in both the velocity difference and in the shear-layer thickness. All these parameters are included in the definition of the bulk Richardson number, and relative changes between these scales are complicated and difficult to predict so that this number is much more sensitive to changes in both the density difference and the water depth, as also demonstrated in figure 11(*c*). The generation of the large-scale surges in the lower layer, on the other hand, is triggered by the pulsating barotropic component and is influenced by changes in the water depth, rather than by the buoyant acceleration. This explains why the Reynolds number is more appropriate for predicting the growth of the length scales compared to the Richardson number.

5. Conclusions

Stratified exchange flows over a fixed obstacle are common in environmental and geophysical flows. The study of the flow processes involved with such flows is important in environmental and ecological studies such as water-quality modelling and pollution remediation. The flow processes related to such flows are the result of purely baroclinic effects, and related interfacial instabilities, possibly with superimposed pulsating external forces, which can be provided, for example, by astronomical or metereological tides or other basin oscillations.

In this paper, a detailed experimental investigation of a two-layer density-stratified exchange flow over a submerged smooth sill has been performed, using a PIV measurement technique. Different starting conditions for the experiment have been examined showing that it is difficult, if not impossible, to avoid completely the superposition of an additional barotropic oscillation onto the baroclinic exchange flow.

A simplified model of barotropic oscillations superimposed on exchange flows has been adapted for the experimental conditions presented. The model can predict the flow-rate oscillations and the related period, given the geometrical and experimental conditions. The model was validated with the experimental results presented here and with the results of Morin *et al.* (2004).

https://doi.org/10.1017/S0022112007008324 Published online by Cambridge University Press

Owing to the superimposed barotropic oscillation, large-scale billows at the interface were observed during the experiments. These billows took the form of pulsating surges to balance the overflow from one water body to the other. This type of instability at the interface has been observed in prior studies (Pawlak & Armi 2000; Morin *et al.* 2004; Fouli 2006), but has not been analysed in detail. The period of generation of these instabilities has been shown to be of the same order of magnitude as the period of oscillation of the net flow rate.

Results for five experiments have been further examined to show the impact of the flow pulsation on the development of the flow. Spectral slopes of the velocity fluctuations of $-7/3$ have been reported for smaller frequencies, along with slopes of $-5/3$ in the last part of the spectrum for higher frequencies. These different slopes suggest the presence of two-dimensional structures which decay in higher frequencies as the turbulence becomes more isotropic. The spectral distributions of the velocity fluctuations in horizontal and vertical directions also show differences of one order of magnitude in the energy values. This is more evident for the experiments with a lower Reynolds number (cf. figure 9).

The ratio $u'/\Delta U$, which gives the response of the velocity fluctuations to the velocity difference increase due to the acceleration down the sill, has revealed an overall increase in longitudinal direction which demonstrates that the overall region studied is characterized by growing turbulence. These results differ from the results of Koop & Browand (1976) and Pawlak & Armi (2000), who reported a decaying rate in the longitudinal direction of $x^{-3/4}$.

The vertical and horizontal length scales of the observed large-scale breaking waves have been estimated using the time scale obtained from the correlation functions of the velocity fluctuations and the convective velocity $\Delta U/2$ (cf. figure 11). Both the vertical and horizontal scales increase with increasing water depth, but slightly decrease with increasing buoyant acceleration for $Re_* = \sqrt{g'H}H/\nu < 60\,000$. This Reynolds number has been shown to be the key parameter governing the generation, development and growth of the interfacial instabilities for stratified exchange flows with superposed pulsating barotropic component. Considering the overall behaviour, it could be concluded that for increasing Re_*, the scales show an increase and the relation $L_I/H = \kappa Re_*$ has been proposed, κ being 9×10^{-6} for the horizontal scales and 3.2×10^{-6} for the vertical scales.

The authors would like to thank the German Science Foundation (DFG Ji 18/12-1) for its support in conducting this research.

REFERENCES

Armi, L. 1986 The hydraulics of two flowing layers with different densities. *J. Fluid Mech.* **163**, 27–58.

Armi, L. & Farmer, D. M. 1986 Maximal two-layer exchange through a contraction with barotropic net flow. *J. Fluid Mech.* **164**, 27–51.

Baines, P. G. 1975 Entrainment by a plume or a jet at a density interface. *J. Fluid Mech.* **68**, 309–320.

Baines, P. G. 1995 *Topographic Effects in Stratified Flows*. Cambridge University Press.

Dean, R. G. & Dalrymple, R. A. 1984 *Water Wave Mechanics for Engineers and Scientists*. Prentice-Hall.

Ellison, T. H. & Turner, J. S. 1959 Turbulent entrainment in stratified flows. *J. Fluid Mech.* **6**, 423–448.

Farmer, D. M. & Armi, L. 1988 The flow of Atlantic Water through the Strait of Gibraltar. *Prog. Oceanogr.* **21**, 1–105.

https://doi.org/10.1017/S0022112007008324 Published online by Cambridge University Press

Farmer, D. M. & Armi, L. 1999 Stratified flow over topography: the role of small scale entrainment and mixing in flow establishment. *Proc. R. Soc. Lond.* A **455**, 3221–3258.

Fernando, H. J. S. 1991 Turbulent mixing in stratified fluids. *Annu. Rev. Fluid Mech.* **23**, 455–493.

Fouli, H. R. S. 2006 An experimental study of interfacial waves and instabilities in exchange flows over a smooth sill. PhD thesis, Department of Civil and Environmental Engineering, Edmonton, University of Alberta.

Hansen, B. & Osterhus, S. 2000 North Atlantic–Nordic Seas exchanges. *Prog. Oceanog.* **45**(2), 109–208.

Helfrich, K. R. 1995 Time-dependent two-layer exchange flows. *J. Phys. Oceanogr.* **25**, 359–373.

Koop, C. G. & Browand, F. K. 1976 Instability and turbulence in a stratified fluid with shear. *J. Fluid Mech.* **24**, 67–113.

Lawrence, G. A. 1993 The hydraulics of steady two-layer flow over a fixed obstacle. *J. Fluid Mech.* **254**, 605–633.

Lawrence, G., Pieters, R., Zaremba, L., Tedford, T., Gu, L., Greco, S. & Hamblin, P. F. 2004 Summer exchange between Hamilton Harbour and Lake Ontario. *Deep-Sea Research II*, **51**, 475–487.

Lien, R.-C., D'Asaro, E. A. & Dairiki, G. T. 1998 Lagrangian frequency spectra of vertical velocity and vorticity in high-Reynolds-number oceanic turbulence. *J. Fluid Mech.* **362**, 177–198.

Morin, V. M., Zhu, D. Z. & Loewen, M. R. 2004 Supercritical exchange flow down a sill. *J. Hydraul. Engng ASCE* **130**, 521–531.

Pawlak, G. & Armi, L. 1998 Vortex dynamics in a spatially accelerating shear layer. *J. Fluid Mech.* **376**, 1–35.

Pawlak, G. & Armi, L. 2000 Mixing and entrainment in developing stratified currents. *J. Fluid Mech.* **424**, 1–37.

Pratt, L. J. 1987 Rotating shocks in a separated laboratory channel flow. *J. Phys. Oceanogr.* **17**, 483–491.

Scinocca, J. F. & Peltier, W. R. 1989 Pulsating downslope windstorms. *J. Atmos. Sci.* **46**, 2885–2914.

Sherwin, T. J. & Turrell, W. R. 2005 Mixing and advection of a cold water cascade over the Wyville Thomson Ridge. *Deep-Sea Res.* **52**, 1392–1413.

Stigebrandt, A. 1977 On the effect of barotropic current fluctuations on the two-layer transport capacity of a constriction. *J. Phys. Oceanogr.* **7**, 118–122.

Stommel, H. & Farmer, H. G. 1953 Control of salinity in an estuary by a transition. *J. Mar. Res.* **12**, 13–20.

Thorpe, S. 1985 Laboratory observation of secondary structures in Kelvin–Helmholtz billows and consequences for ocean mixing. *Geophys. Astrophys. Fluid Dyn.* **35**, 175–199.

Turner, J. S. 1963 Model experiments relating to thermals with increasing buoyancy. *Q. J. R. Met. Soc.* **89**, 62–74.

Welander, M. V. 1984 Flow around circular cylinder-kaleidoscope of challenging fluid phenomena. *Proc. Symp. Fully Separated Flows*, vol. 1, p. 102.

Wüest, A., Imboden, D. M. & Schurter, M. 1988 Origin and size of hypolimnic mixing in Urnersee, the southern basin of Vierwaldstaettersee (Lake Lucerne), Schweiz. *Schweiz. Z. Hydrol.* **50**, 40–70.

Zhu, D. Z. & Lawrence, G. A. 1998 Non-hydrostatic effects in layered shallow water flows. *J. Fluid Mech.* **355**, 1–16.

Zhu, D. Z. & Lawrence, G. A. 2000 Hydraulics of exchange flows. *J. Hydraul. Engng ASCE* **126**, 921–928.

https://doi.org/10.1017/S0022112007008324 Published online by Cambridge University Press